Multiscale interactions of elastic anisotropy in unsaturated clayey rocks using a homogenization model

Sabrina C.Y. Ip¹ · Ronaldo I. Borja^{1,*}

¹Department of Civil and Environmental Engineering, Stanford University, Stanford, CA 94305, USA. *E-mail: borja@stanford.edu

Summary. The microstructure of a geomaterial plays a significant role in determining its macroscale properties. Most clay rocks have an anisotropic microstructure due to preferential orientation of the pores and mineral grains, which results in transverely isotropic mechanical properties. Their anisotropic microstructure is complex and spans multiple orders of magnitudes. The interactions between anisotropy at different scales in these rocks can give rise to emerging properties such as saturation-dependent elastic anisotropy. In this study, we develop a homogenization model with three-levels of upscaling to capture the multiscale interactions of elastic anisotropy in unsaturated clay rocks. The model provides an enriched description of the elastic behavior of clay rocks during changes in the degree of saturation by bridging the nano-, micro- and macroscale microstructures. Stress-point simulations are presented to demonstrate the interactions between anisotropy at different spatial scales that result in the elastic behavior of clay rocks observed in the literature, including constant anisotropy, evolving anisotropy and a rotation of the principal orientation of anisotropy. The results highlight that constant and evolving elastic anisotropy can originate from the same microstructural features that either neutralize or enhance one another. Overall, the proposed model offers a quantitative link between anisotropy at multiple scales in clay rocks and its macroscopic anisotropic stiffness.

Keywords. Anisotropy, elasticity, micromechanics, unsaturated rock mechanics

1 Introduction

Clay rocks, such as mudstones and shale, have a multitude of applications including as the main cap rock of geological formations being considered for anthropogenic CO₂ sequestration [36], as potential host rocks for radioactivate waste repositories [69] and as source rocks of low-carbon fuels [50]. These rocks exhibit structural heterogenities over many orders of magnitude, ranging from

a few nanometers to several meters [55]. The multiscale microstructure of clay rocks have a significant impact on their hydraulic, chemical and mechanical properties [58]. For example, the distribution of nano-pores impacts the gas transport and adsorption/desoprtion behavior [57], while mesoscale pores can include non-Darcy flow and surface diffusion which affects fluid transport behavior [39]. In order to accurately evaluate and predict the behavior of clay rocks in these applications, it is important for models to incorporate their multi-scale and multi-physics microstructure.

The mechanical properties of clay rocks and many other geomaterials are influenced by its microstructure [37, 128]. Clay rocks often exhibit transverse isotropy due to a preferred orientation of pores, cracks and grains along distinct bedding planes arising from deposition, compaction and lithification processes. The elastic properties of these rocks are symmetric about the bedding plane and anisotropic in the bedding normal direction. A number of studies have investigated the anisotropic elastic properties of clay rocks [2, 40, 63, 71, 95, 98, 118] and their incorporation into constitutive models [8, 18, 20, 72, 85, 116, 124, 127] and poro-mechanical responses [123, 125, 126]. Simultaneously, clay rocks can be partially saturated, in which the pores are filled with both air and water. Changes in the degree of saturation can cause the clay rock microstructure to evolve and affect its elastic properties [9, 22, 34, 104, 113]. For example, water-weakening of the Young's modulus has been observed in various shales during hydration [3, 112, 113]. Furthermore, interactions between the degree of saturation and anisotropy can result in saturation-dependent elastic anisotropy and strain anisotropy. The Young's modulus in the bedding parallel direction has been observed to be more sensitive to changes in the degree of saturation [27, 42, 98, 119, 121]. As a result, stiffness anisotropy generally becomes more pronounced upon desaturation of clay rocks [27, 64, 82, 98, 118, 121]. Several authors have also reported strain anisotropy during drying tests of geomaterials [67, 80], which generally also increases with dehydration.

Several micromechanisms that contribute to saturation-dependent elastic anisotropy have been proposed. Clay particles stiffen during dehydration due to thinning of the water film and chemical hardening [118]. Yurikov et al. found that these clay particles were strongly aligned along the bedding plane and suggested that the orientation caused a preferential strengthening of the shale in the bedding parallel direction. The evolution of the pore microstructure could also contribute to evolving anisotropy. The closing of microcracks and bedding planes as suction increases could cause the shale to stiffen in a preferential direction [119]. Suction could also change the pore shape and pore aspect ratio. Yurikov et al. highlighted that the pores in Opalinus clay were becoming stiffer in the tangential direction upon dehydration [118]. Nonetheless, there is a lack of in-depth understanding into the physics and their interactions between multiple scales that contribute to evolving anisotropy in clay rocks.

Hydromechanical frameworks have been developed for modeling saturationdependent elastic anisotropy and strength anisotropy [44, 45]. These models use constitutive models based on empirical relationships obtained from measured data between stiffness/strength properties and saturation. However, empirical models overlook the interactions between the various physics involved and lack insight into the micromechanics that gives rise to evolving anisotropy at the macroscale. On the other hand, homogenization models can embed information from multiple microstructural levels and provide a deeper understanding of the multi-scale physics interactions that give rise to emerging properties. Homogenization approaches are based on the concept of the Representative Elementary Volume (REV), which differentiates between the space scales, and is the volume of heterogeneous material that is sufficiently large to be statistically representative of the upper space scale. Within the REV, geomaterials can be idealised as a composite material comprising inclusions (with varying shapes, orientations and material properties) embedded in a host matrix. The average-field theory can then be utilized to derive the effective mechanical properties of the REV.

The multiscale nature of shales have been widely explored in the literature through the use of homogenization models [5, 10, 16, 19, 41, 52, 74, 75, 83, 87– 89, 101, 122. Hornby [41] and Sayers [83] both adopted a homogenization model with a clay-particle orientation distribution function to characterize anisotropic elastic wave velocity measurements. Recently, Zhang et al. developed a model considering the depositional layering tendency of inclusion minerals in shale [122]. Homogenization models for unsaturated materials with porosities at multiple scales have also been developed [14, 15, 24–26, 28]. These models generally focused on isotropic porous materials. Mainka et al. [61] formulated a multiscale stress description of clay particles with micropores and partial saturation using a homogenization method for a periodic microstructure. Chateau & Dormieux tackled the micromechanics of unsaturated materials and accounted for the effects of surface tension [14]. Cariou et al. addressed the multi-scale microstructure of unsaturated Callovo-Oxfordian shale using a three-level homogenization model [10]. However, the interactions between anisotropy and partial saturation across multiple scales has rarely been considered [10, 28].

Several microstuctural levels have been identified as relevant to the mechanical and unsaturated behaviors in clay rocks [5, 10, 86, 97]. In order of increasing magnitude, these include (1) the scale of elementary clay platelets, (2) the scale of elementary clay platelets stacked together to form clay particles, (3) the submicrometer scale of an assembly of clay particles forming a clay matrix, (4) the submillimeter scale in which the clay matrix is intermixed with detrital grains (mainly quartz and calcite) and (5) the scale of alternating clay-rich and detrital layers resulting of depositional layering.

In this study, we propose a three-step homogenization model that focuses on scales (2) through (4). The model employs volume averaging techniques to bridge the nano-, micro- and macroscale microstructures of clay rocks and

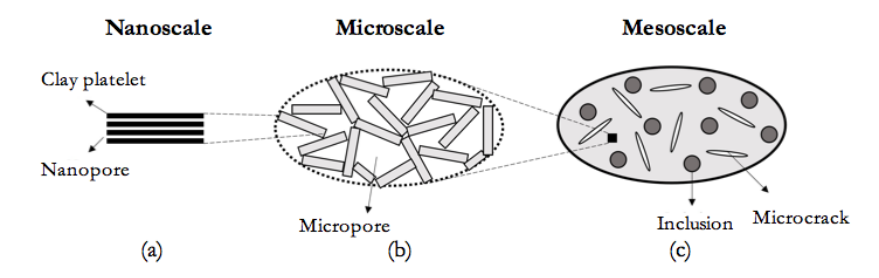


Fig. 1. Three-step homogenization model incorporating the microstructure of clay rocks. (a) Nanoscale: clay particle comprising clay platelets and nanopores; (b) Microscale: Assembly of clay particles and micropores; (c) Macroscale: Clay matrix surrounding inclusions and microcracks

it provides an enriched constitutive relationship for the elastic behavior of clay rocks. We conduct stress-point simulations of drying tests on several clay rocks, including Callovo-Oxfordian shale, Opalinus clay and Tage tuff, to highlight its ability to capture constant anisotropy, evolving anisotropy and a rotation of the principal orientation of anisotropy. The model gives insight into the roles of evolving microstructure at various scales on the macroscopic elastic properties of clay rocks.

2 Theory

This section presents a three-step upscaling scheme, detailed in Figure 1, to capture the effects of shale microstructure at multiple scaless on its anisotropic elastic properties. At the nanoscale, we consider the REV to be a clay particle, which comprises clay platelets stacked on top of one another with the interlayer space saturated with water. At the microscale, the REV is the porous clay matrix consisting of clay particles arranged in a preferred orientation pattern and micropores. Finally, at the macroscale, the porous clay matrix surrounds inclusions such as quartz and calcite, as well as microcracks which open and close with changes in the degree of saturation. In the following sections, the superscripts n, μ , M are used to refer to the nanoscale, microscale and macroscale, respectively, and the superscripts l, g, p are used to represent the liquid phase, gaseous phase and pore space, respectively. We note that the proposed model assumes that the pore fluids at all scales are in equilibrium (ie. no fluid flow between pores of different scales) and that there are no interactions between the nano- and micro-porosities.

2.1 Nanoscale

A clay particle can be idealised as multiple layers of parallel clay platelets with interlayer spaces in between each platelet (Figure 1a). In the following sec-

tions, the platelet (solid) phase is denoted by superscript s and the interlayer (fluid) space is denoted by superscript f.

The interlayer space is filled with interlayer water and exchangeable cations. As a result, in addition to mechanical and hydraulic forces, there are electrochemical forces present at the nanoscale. These electrochemical forces can be significant due to the small distance (on the order of nanometers) between clay platelets. We assume the interlayer water can be modeled as a continuous liquid (as compared to discrete water molecules) and the interlayer space is always saturated with fluid. The interlayer distance, h, can be obtained from the (Eulerian) nanoporosity, ϕ^n , through the following relationship [23, 117]

$$h = \frac{2\phi^n}{\rho_c SSA(1 - \phi^n)}, \qquad (1)$$

where ρ_c is the solid density of the clay platelets (assumed to be 2.6 g/cm³) and SSA is the specific surface area.

Interlayer water

The surfaces of clay minerals are generally negatively charged and will interact with the exchangeable cations in the pore fluid, giving rise to an electrical potential distribution around the clay platelet which can be described by the Gouy-Chapman theory [13, 68]. Overlapping of the electrical potential distributions as two clay platelets approach each other results in a repulsive double layer force in the interlayer space. The repulsive force depends on the interlayer distance, the ionic concentration and the ionic valence. Previous studies have derived the double layer force per unit area between two parallel clay platelets as [46, 49, 68]

$$\pi^{\text{DDL}} = 2nkT(\cosh(u) - 1), \qquad (2)$$

where

$$u = 8\tanh^{-1}\left(\exp(-\kappa h)\tanh\left(\frac{z}{4}\right)\right),$$

$$\kappa = \sqrt{\frac{2nv^2e'^2}{\varepsilon kT}},$$

$$z = 2\sinh^{-1}\left(\frac{\text{CEC}}{\text{SSA}}\sqrt{\frac{1}{8\varepsilon nkT}}\right),$$
(3)

CEC is the cation exchange capacity, SSA is the specific surface of the clay platelet, ε is the static permittivity of the water solution, n is the ion concentration in the pore water, k is the Boltzmann constant $(1.38 \times 10^{-23} \text{ J/°K})$, T is the absolute temperature (assumed to be 293.15°K), e' is the electric charge $(1.602 \times 10^{-19} \text{ C})$ and v is the ionic valence. In this study, we assume constant values of v=1, CEC = 0.732 mEq/g and $\varepsilon=7.083 \times 10^{-10}$ C²/(J

 \cdot m) [41, 49]. We also note that the ionic concentration is assumed to remain constant throughout the drying process and geochemically-induced shrinkage is not considered in this work.

In addition to the double layer forces, it is well known that attractive van der Waals forces exist between two molecules in close distance to each other. Similar to the double layer force, this attractive force increases with decreasing interlayer distance. The van der Waals force for two parallel layers [12, 49] was derived from London's theory for the attractive stress between two molecules [54] and is given by

$$\pi^{\text{VDW}} = \frac{A_h}{24\pi} \left(\frac{1}{(h/2)^3} + \frac{1}{(h/2 + t)^3} - \frac{2}{(h/2 + t/2)^3} \right),\tag{4}$$

where t is the thickness of the clay mineral crystals, which we assume to be 0.96 nm, and A_h is the Hamaker constant which has a value of 2.2×10^{-21} J for montmorillonite from theoretical analysis of coagulation measurements [73].

Since the interlayer space remains fully saturated, the stress in the interlayer water can be described by a liquid pressure p^l and an overpressure $(\pi^{\text{DDL}} - \pi^{\text{VDW}})$ acting in the normal direction to the clay platelets \boldsymbol{n} :

$$\boldsymbol{\sigma}^f = -p^l \mathbf{1} - (\boldsymbol{\pi}^{\text{DDL}} - \boldsymbol{\pi}^{\text{VDW}}) \boldsymbol{n} \otimes \boldsymbol{n}.$$
 (5)

Using a first-order Taylor's series expansion and defining the fluid strain as $\epsilon^f = dh/h_0 \mathbf{n} \otimes \mathbf{n}$, we can write a constitutive law for the interlayer water as

$$\boldsymbol{\sigma}^f = \mathbb{C}^f : \boldsymbol{\epsilon}^f + \boldsymbol{\sigma}_p^f, \tag{6}$$

where

$$\mathbb{C}^{f} = -h_{0}K^{f}\boldsymbol{n} \otimes \boldsymbol{n} \otimes \boldsymbol{n} \otimes \boldsymbol{n},$$

$$K^{f} = \frac{\partial \boldsymbol{\pi}^{\text{DDL}}}{\partial h} \Big|_{h_{0}} - \frac{\partial \boldsymbol{\pi}^{\text{VDW}}}{\partial h} \Big|_{h_{0}},$$

$$\boldsymbol{\sigma}_{p}^{f} = -p^{l}\mathbf{1} - (\boldsymbol{\pi}^{\text{DDL}}|_{h_{0}} - \boldsymbol{\pi}^{\text{VDW}}|_{h_{0}})\boldsymbol{n} \otimes \boldsymbol{n},$$
(7)

and h_0 is the interlayer distance in the initial configuration.

Clay particle

The stress tensor at the nanoscale (in the clay particle) can be written as

$$\boldsymbol{\sigma}^n = \mathbb{C}(\boldsymbol{x}) : \boldsymbol{\epsilon}^n + \boldsymbol{\sigma}_n^n(\boldsymbol{x}), \tag{8}$$

in which

$$\mathbb{C} = \begin{cases}
\mathbb{C}^s \\
\mathbb{C}^f
\end{cases}, \qquad \boldsymbol{\sigma}_p^n = \begin{cases}
\mathbf{0} & \text{in } \Omega^s \\
\boldsymbol{\sigma}_p^f & \text{in } \Omega^f
\end{cases},$$
(9)

 \mathbb{C} is the nanoscale stiffness tensor, σ_p^n is the nanoscale prestress tensor (also known as the eigenstress), ϵ^n is the nanoscale strain tensor and x is the position vector in the REV domain Ω . We assume the clay platelets are incompressible ($\nu \to 0.5$).

Levin theorem [51] allows us to obtain a continuous representation of the stress field at the nanoscale by the following equation

$$\Sigma^n = \mathbb{C}^n : E^n + \Sigma_p^n \,, \tag{10}$$

where the homogenized nanoscale stiffness $\underline{\operatorname{tensor}} \ \mathbb{C}^n = \overline{\mathbb{C} : \mathbb{A}}$, the homogenized nanoscale prestress tensor $\boldsymbol{\mathcal{L}}_p^n = \overline{\boldsymbol{\sigma}_p : \mathbb{A}}, \ \boldsymbol{\mathcal{L}}^n$ is the homogenized nanoscale strain tensor, $\boldsymbol{\mathcal{E}}$ is the strain concentration tensor, and $\overline{(\cdot)}$ represents the volume average. We also adopt a Mori-Tanaka homogenization scheme [38], where the averaged concentration tensors in phase p (p=s,f) can be expressed as:

$$\mathbb{A}^p = (\mathbb{I} + \mathbb{P} : (\mathbb{C}^p - \mathbb{C}^s))^{-1} : \overline{(\mathbb{I} + \mathbb{P} : (\mathbb{C} - \mathbb{C}^s))^{-1}}^{-1},$$
(11)

where \mathbb{P} is the Hill tensor that depends on the matrix properties and the shape and orientation of the inclusions.

The interlayer spaces are idealised as oblate spheroids with small aspect ratio, ξ , that tends to 0 ($\xi \to 0$). Using the results of [28], the homogenized (symmetric) stiffness matrix of the clay particle can then be written as

$$[\mathbb{C}^n] = \begin{bmatrix} c_1 & c_3 & c_4 & 0 & 0 & 0 \\ \cdot & c_1 & c_4 & 0 & 0 & 0 \\ \cdot & \cdot & c_2 & 0 & 0 & 0 \\ \cdot & \cdot & \cdot & 2c_5 & 0 & 0 \\ \cdot & \cdot & \cdot & \cdot & 2c_5 & 0 \\ \cdot & \cdot & \cdot & \cdot & \cdot & 2c_6 \end{bmatrix},
 (12)$$

where

$$c_{1} = \frac{1 - \phi^{n}}{\phi^{n}} ((1 - \phi^{n})K^{f} + 3\phi^{n}\mu) + 2(1 - \phi^{n})\mu,$$

$$c_{2} = \frac{K^{f}}{\phi^{n}},$$

$$c_{3} = \frac{1 - \phi^{n}}{\phi^{n}} ((1 - \phi^{n})K^{f} + 3\phi^{n}\mu) - 2(1 - \phi^{n})\mu,$$

$$c_{4} = \frac{1 - \phi^{n}}{\phi^{n}}K^{f},$$

$$c_{5} = 0,$$

$$c_{6} = 2(1 - \phi^{n})\mu,$$
(13)

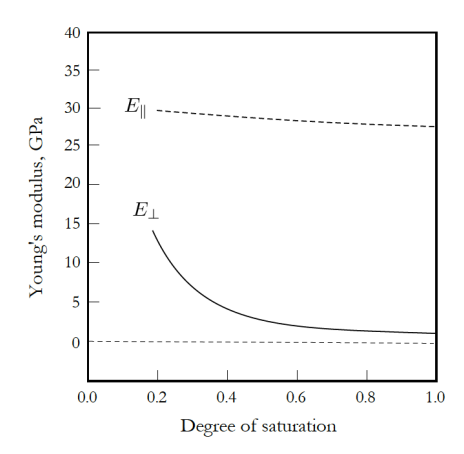


Fig. 2. Variation of Young's moduli in the normal (E_{\perp}) and parallel (E_{\parallel}) directions with degree of saturation for a single clay particle.

 μ is the shear modulus of the clay platelets and ϕ^n is the porosity at the nanoscale. We note that the shear stiffness of the clay particle in the parallel direction is 0 since the platelets can slide over each other. The prestress of the clay particle can be expressed as

$$\delta \Sigma_p^n = -\delta p^l \mathbf{1} - \left(\delta \pi^{\text{DDL}} - \delta \pi^{\text{VDW}}\right) (\mathbf{1} - \phi^n (\mathbf{1} - \boldsymbol{n} \otimes \boldsymbol{n})).$$
(14)

To illustrate the anisotropic elastic properties of a single clay particle, Figure 2 presents the Young's moduli in the directions normal and parallel to an illite platelet. The following material parameters are assumed: saturated nanoporosity of $\phi^n = 0.08$, SSA = 83 m²/g, n = 20 mol/m³ and $\mu = 10$ GPa. The value of SSA was estimated by Macht et al. [60] from atomic force microscopy tests; n was taken from the values used in Komine and Ogata [49]; and μ was taken from Hornby et al. [41] based on their back-calculation from a Greenhorn shale whose clay fraction comprises mainly of illite and smectite. We observe water-weakening of the clay particle. Upon drying, the interlayer distance shrinks, which results in stiffening of the interlayer water and the entire clay particle. The stiffening of the interlayer water also causes a decrease in the elastic anisotropy upon drying, unlike the observed behavior of clay rock samples. The decrease in the elastic anisotropy ratio during drying is corroborated by molecular dynamic simulations of clay particles with varying water content [11].

2.2 Microscale

The REV at the microscale is an assembly of clay particles and a network of interparticle pores, herein referred to as micropores. The micropore network

is assumed to be partially saturated by the same pore fluid as the nanopores. We assume that the pore fluids at multiple scales are in equilibrium with one another, and so the pore pressures are the same at all scales. Several authors have highlighted that the micropores geometry in shales can be approximated with oblate spheroids of varying aspect ratios ranging from less than 0.05 to between 0.5 and 1 [92, 101, 102]. Furthermore, the clay particles are typically preferentially oriented along the bedding plane [21, 41, 56, 88, 103, 108]. Hence, we model the clay matrix as an aggregate formed by preferentially oriented clay particles and spheroidal micropores aligned with the bedding plane.

Several models have been developed to describe the preferential orientation of clay platelets with respect to the bedding plane [1, 47, 62, 76, 83]. In this study, we adopt the Owens-March orientation distribution function (ODF) [56]

$$ODF(\theta) = \frac{MPD}{[\cos^2(\theta) + MPD\sin^2(\theta)]^{1.5}},$$
(15)

where θ is the angle between the clay particle normal direction and the bedding plane normal and the maximum pole density (MPD) is a parameter measured in logarithmic scale from 1.0 to ∞ . MPD = 1.0 for a random distribution of clay particles and MPD = ∞ for perfectly aligned clay particles.

The effective stiffness and effective prestress of the clay particles aligned with respect to the bedding plane can be obtained from the following integral

$$\mathbb{C}^{av} = \frac{1}{8\pi^2} \int_0^{2\pi} \int_0^{2\pi} \int_0^{\pi} \text{ODF}(\theta) \mathbb{C}^{n}(\theta, \psi, \phi) \sin(\theta) \, d\theta \, d\psi \, d\phi ,$$

$$\mathbf{\Sigma}_p^{av} = -p^l \mathbf{1} - (\pi^{\text{DDL}} - \pi^{\text{VDW}}) \Big[(1 - \phi^n) \mathbf{1} + \phi^n \frac{1}{8\pi^2} \int_0^{2\pi} \int_0^{2\pi} \int_0^{\pi} \text{ODF}(\theta) \mathbf{n} \otimes \mathbf{n} \sin(\theta) \, d\theta \, d\psi \, d\phi \Big] ,$$
(16)

where θ , ψ and ϕ are Euler angles [77].

We consider the micropore geometry to be oblate spheroids with an aspect ratio $\xi = l_{min}/l_{max}$, where l_{min} and l_{max} are the minimum and maximum principal radii, respectively. The micropores are also assumed to be perfectly aligned along the bedding plane.

At this scale, the micropores are filled with both water and air. The forces contributing to the prestress include the water and air pressures, p^l and p^g and the surface tensions at the interfaces, γ^{ab} , where a, b = s, l, g represent the solid, liquid and gas phases.

The membrane stress tensor can be expressed as

$$\omega^{ab} = \gamma^{ab} (\mathbf{1} - \hat{\boldsymbol{n}} \otimes \hat{\boldsymbol{n}}), \qquad (17)$$

where $\hat{\boldsymbol{n}}$ is the unit normal vector at a point on the interface between two phases [14].

The state equation of the clay matrix can be then written as

$$\mathbb{C} = \begin{cases}
\mathbb{C}^{av} \\
\mathbb{O} \\
\mathbb{O}
\end{cases}, \quad \boldsymbol{\sigma}_{p}^{\mu} = \begin{cases}
\boldsymbol{\sigma}_{0}^{matrix} + \boldsymbol{\Sigma}_{p}^{av} & \text{in } \Omega^{\text{matrix}} \\
-p^{l} \mathbf{1} & \text{in } \Omega^{l} \\
-p^{g} \mathbf{1} & \text{in } \Omega^{g} \\
\omega^{ab} & \text{in } \Gamma^{\text{ab}}
\end{cases}, \quad (18)$$

where \mathbb{O} is a fourth-order null tensor, σ_0^{matrix} is the initial prestress in the matrix, and Γ represents the surfaces in the domain between two different phases.

The homogenized macroscopic stiffness and prestress of the clay matrix can again be obtained using Levin theorem [51] as

$$\mathbb{C}^{\mu} = \mathbb{C}^{av} - \phi^{\mu} \mathbb{C}^{av} : \mathbb{A}^{p},
\delta \mathbf{\Sigma}_{p}^{\mu} = -\phi^{\mu} \delta \bar{p} \mathbf{1} : \mathbb{A}^{p}
+ (1 - \phi^{\mu}) \delta \mathbf{\Sigma}_{p}^{av} : \mathbb{A}^{m} + \delta \overline{\omega^{ab}} : \mathbb{A}^{p},$$
(19)

where $\bar{p} = \psi^l p^l + \psi^g p^g$, \mathbb{A}^p and \mathbb{A}^m are the strain concentration tensors representing the micropore phase and the clay particle matrix phase, respectively. Appendix A.1 presents the Hill tensor for oblate spheroidal inclusions aligned along the bedding plane in a transversely isotropic host matrix.

Water retention curve

In the unsaturated regime, a water retention law is needed to characterize the relationship between the degree of saturation and the suction. To differentiate between water in the interlayer space and water in the micropores, we adopt a water retention model that includes the effect of bound and capillary water. To this end, we consider the work of Revil & Lu (2013) [81], who described the water content as the sum of bound and trapped water, θ_a and capillary water, θ_c , both of which are functions of suction, s.

$$\theta(s) = \theta_c(s) + \theta_a(s). \tag{20}$$

The capillary water content is modeled with the van Genuchten retention model [99], while the adsorbed water is modeled with the Freundlich sorption isotherm [32]

$$\theta_c(s) = \frac{\theta_{sat} - \theta_a}{\left[1 + (\alpha s)^n\right]^{1 - 1/n}},$$

$$\theta_a(s) = \theta_a^{\max} \left[\exp\left(-\frac{M_v}{RT}s\right)\right]^{1/m_{ads}},$$
(21)

where α is the inverse of the scaling suction, n is a van Genuchten parameter, m_{ads} is a Freundlich adsorption isoterm coefficient representing the adsorption

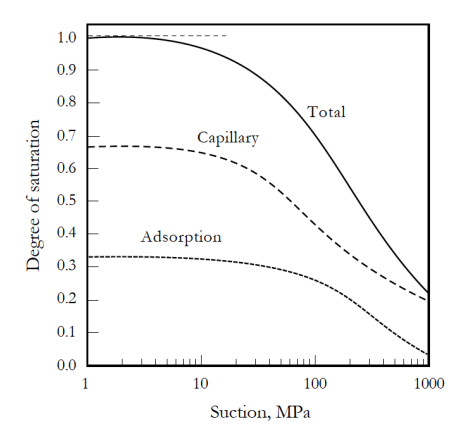


Fig. 3. Adsorbed, capillary, and total water retention curves.

strength, θ_a^{\max} is the maximum adsorbed water content, θ_{sat} is the saturated volumetric water content, M_v is the molar volume of water, R is the universal gas constant and T is the absolute temperature. The degree of saturation can then be expressed as

$$\psi^w(s) = \frac{\theta_c(s) + \theta_a(s)}{\theta_{sat}}.$$
 (22)

Figure 3 presents an example water retention curve of the model adopted in this study with the following parameters: $\theta_{sat} = 0.15$, $\theta_a^{\max} = 0.05$, $\alpha = 40$ MPa, n = 1.5, $m_{ads} = 3$.

Contribution of surface tension

The effect of surface tension on the mechanical behavior of the REV is difficult to quantify as it requires knowledge of porous network and the interface geometry. Thus, we use a simplified method to quantify the surface tension term and highlight that its contribution to the prestress is small.

The pore network has been previously idealised as a set of spheres in the literature [10]. In such a porous network, the pores can be divided into two sets: pores fully filled with either water or air. The delineation between these two sets is governed by Laplace relation and the radius of the pore. At a given suction, small pores would be filled with water, while water in large pores would have drained and they would be filled with air. The threshold radius can be calculated from the Laplace equation of capillarity as [114]

$$r^* = \frac{2\gamma^{lg}\cos(\Theta)}{s} \,. \tag{23}$$

where Θ is the contact angle.

Since the pores in the proposed model are oblate spheroids, we use the equivalent minimum harmonic mean radius, $r_{eq} = (0.5(l_{max}^{-1} + (\xi l_{max})^{-1}))^{-1}$

to obtain a relationship between the set of pores filled with air and the suction [114, 115]. The pore size distribution function (PSD) can be deduced from the capillary water retention curve. An example PSD obtained from the water retention curve in Figure 3 is presented in Figure 4a, assuming the surface tension between the air and water phases to be $\gamma^{lg} = 72.5 \text{ mN/m}$ and $\xi = 0.05$.

Following the derivation of Chateau & Dormieux [14], the surface tension term can then be expressed as

$$\overline{\omega^{ab}: \mathbb{A}^p} = \frac{p^{eq}\phi^{\mu}}{\Omega^p} \int_{\Gamma^p} (\mathbf{1} - \hat{\boldsymbol{n}} \otimes \hat{\boldsymbol{n}}) : \mathbb{A}^p d\Gamma, \qquad (24)$$

where p^{eq} is the equivalent pressure in the micropores, defined as

$$p^{eq} = \int_{r_{min}}^{r_{max}} p^{\gamma}(r_{eq}) PSD(r_{eq}) dr_{eq}, \qquad (25)$$

 r_{min} and r_{max} are the minimum and maximum pore radii, respectively, and PSD is the pore size distribution function, which can be obtained from the water retention curve and

$$p^{\gamma}(r_{eq}) = \begin{cases} 2\gamma^{sl}/r_{eq} & r_{eq} < r^* \\ 2\gamma^{sg}/r_{eq} & r_{eq} \ge r^* \end{cases}$$
 (26)

We note that as the pores are spheroidal, analytical integration of the expression for $\hat{\boldsymbol{n}} \otimes \hat{\boldsymbol{n}}$ is complicated and the surface tension is obtained by numerical integration.

We simulated a shrinkage test of a fully saturated sample to 20% saturation to elucidate the contribution of the surface tension term. The water retention curve and PSD function in Figures 3 and 4 are used in the simulation. The

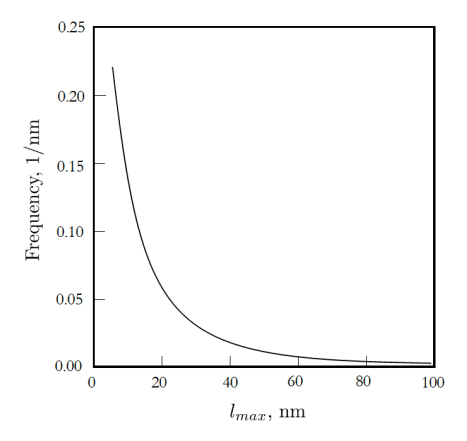


Fig. 4. Pore size distribution function deduced from the capillary water retention curve (Figure 3).

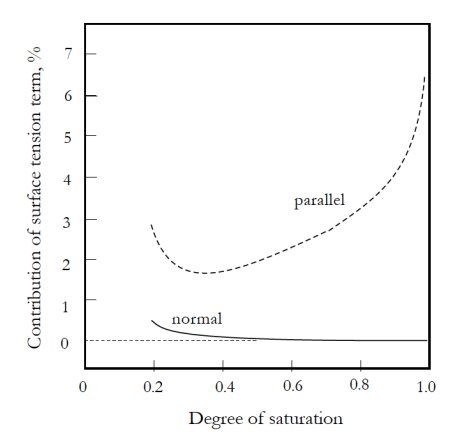


Fig. 5. Contribution of the surface tension term in the bed-parallel and bed-normal directions as a percentage of the total prestress.

solid phase was assumed to be perfectly wetting (i.e., $\gamma^{sl}=0$) and the surface tension between the solid and gas phases and the liquid and gas phases are assumed to be equivalent (i.e., $\gamma^{sg}=\gamma^{lg}=72.5~\text{mN/m}$). The material parameters are selected as SSA = $20~\text{m}^2/\text{g}$, $n=50~\text{mol/m}^3$, $\mu=10~\text{GPa}$ and MPD = 2~[41, 49]. Figure 5 presents the surface tension term in the bedding normal and bedding parallel directions as a percentage of the prestress. We observe that the surface tension contribution has a large anisotropy between the bedding normal and bedding parallel directions. This is due to the small aspect ratio of the pores and the pores being aligned with the bedding plane, which results in much larger surface tension in the bedding parallel direction. The bedding normal surface tension is negligible while the bedding parallel surface tension is generally small.

2.3 Macroscale

At the microscale, the proposed constitutive model represents a clay matrix. However, it still lacks important features of clay rocks such as shale, namely, the presence of inclusions such as quartz and calcite, as well as microcracks. At this scale, the volume fraction of the matrix, inclusions and the microcracks must sum to one:

$$\phi^M + \phi^{inc} + \phi^{matrix,\mu} = 1. \tag{27}$$

Many have proposed that hydration facilitates the propagation of microcracks in shale [34, 53, 78, 100, 104, 106, 113], which can give rise to water-weakening behavior [113]. We consider the microcracks to exhibit an oblate spheroidal shape with a low aspect ratio ($\xi = 0.01$) and that they are randomly distributed in the shale sample. These microcracks are assumed to close upon drainage and as such, there is no surface tension term at the macroscale. As

quantitative information on these microcracks is generally lacking, we assume that the volume fraction of microcracks in the sample (ϕ^M) varies linearly with the degree of saturation and the sample has no microcracks when fully dry $(\phi^M = 0)$.

The state equation of the shale can be written in a similar manner to that of the clay matrix in the previous homogenization step:

$$\mathbb{C} = \begin{cases}
\mathbb{C}^{\mu} \\
\mathbb{C}^{inc}, & \boldsymbol{\sigma}_{p}^{M} = \begin{cases}
\boldsymbol{\sigma}_{0} + \boldsymbol{\Sigma}_{p}^{\mu} & \text{in } \Omega^{\text{matrix}} \\
\boldsymbol{\sigma}_{0} & \text{in } \Omega^{\text{inc}} \\
-p^{l} \mathbf{1} & \text{in } \Omega^{l}
\end{cases} ,$$
(28)

where \mathbb{C}^{inc} is the elasticity tensor for the inclusion phase, σ_0 is the initial stress in the shale under conditions of no strain and no suction.

Levin theorem once again gives the homogenized macroscopic stiffness and pre-stress of the shale:

$$\mathbb{C}^{M} = \mathbb{C}^{\mu} - \phi^{M} \mathbb{C}^{\mu} : \mathbb{A}^{p} + \phi^{inc} (\mathbb{C}^{inc} - \mathbb{C}^{\mu}) : \mathbb{A}^{inc} ,$$

$$\delta \boldsymbol{\Sigma}_{p}^{M} = -\phi^{M} \delta p^{l} \mathbf{1} : \mathbb{A}^{p}
+ (1 - \phi^{M} - \phi^{inc}) \delta \boldsymbol{\Sigma}_{p}^{\mu} : \mathbb{A}^{m} ,$$
(29)

where \mathbb{A}^p , \mathbb{A}^{inc} and \mathbb{A}^m are the strain concentration tensors representing the microcrack phase, inclusion phase and the clay matrix phase, respectively. Appendix A.2 presents the Hill tensor for oblate spheroidal inclusions randomly distributed in a transversely isotropic host matrix.

The proposed constitutive model can be integrated into numerical simulation codes to solve coupled initial boundary value problems for anisotropic porous media [42, 44]. The model only needs the degree of saturation at a material point to determine a relation between macroscopic stress and macroscopic strain in the material that considers the influence of heterogeneous features at lower scales. The degree of saturation at each node can be obtained by solving for the pore pressure in a coupled boundary value problem and using the water retention curve. Along with constraints on the stresses and/or strains at the boundaries, the boundary value problem can then be solved to obtain the local fields of macroscopic stress and strain. We note that the Mori-Tanaka homogenization scheme adopted in the proposed model has been shown to provide consistent results regardless of the type of boundary condition applied (uniform stress or uniform strain) [70].

3 Evolving microstructure

The behavior of various clay rocks during drying tests have been reported in the literature [43, 59, 80, 93, 98]. In this section, we simulate a series of drying tests at the stress-point level to demonstrate the capability of the

proposed model in capturing the behavior of clay rocks during drying tests, including constant anisotropy [79], evolving anisotropy [118] and a rotation of the principal orientation of anisotropy [95].

3.1 Influence of micropore aspect ratio

We elucidate the effect of an evolving microstructure at the microscale in the form of varying pore aspect ratio during drying. Suction has been observed to change the pore size distribution function and the pore shape [9, 22, 84, 90, 94]. After drainage of a pore, its aspect ratio may decrease. We simulated a shrinkage test of a fully saturated clay sample to 40% saturation consider two cases: (1) no evolution in the pore aspect ratio and (2) a decrease in the pore aspect ratio by 50%. The water retention curve in Figure 3 was used in the simulation. The following material parameters were also used: SSA = 50 m^2/g , $n = 40 \, \text{mol/m}^3$, $\mu = 10 \, \text{GPa}$, $\xi = 0.05$. In the case with evolving aspect ratio, the pore aspect ratio would decrease to $\xi = 0.025$ after drainage of a pore.

Figure 6 presents variations in the Young's moduli and the elastic anisotropy ratio with the degree of saturation for both cases. We observe that the Young's modulus in the bedding parallel direction is similar in both cases, while the bedding normal Young's modulus differ as the saturation decreases. This is due to the micropores being aligned with the bedding plane, so changes in the aspect ratio have a strong influence on the bedding normal compliance, but have little effect in the bedding parallel direction. In the bedding normal direction, the sample with evolving microstructure exhibits a decrease in Young's modulus upon desaturation. We note that while clay

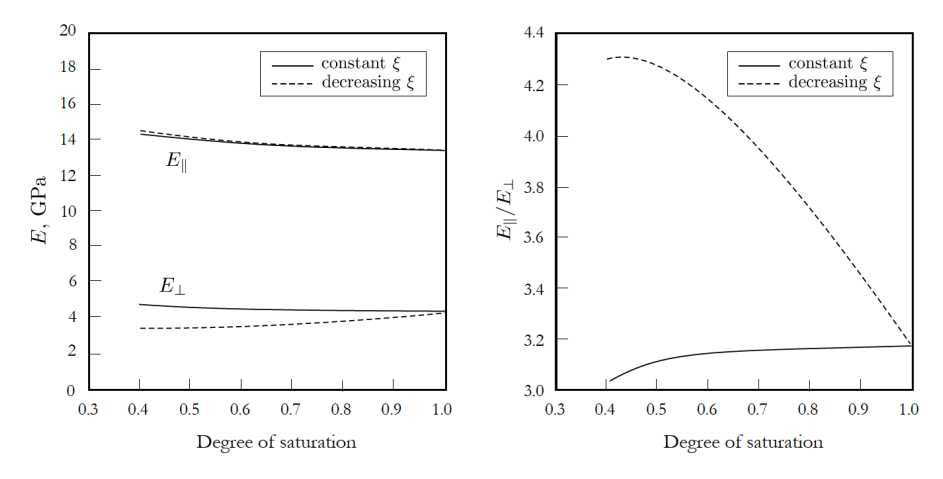


Fig. 6. Effect of evolving micropore aspect ratio on Young's moduli (left) and elastic anisotropy (right) during a drying test.

rocks generally exhibit water-weakening, the opposite behavior has also been recorded in the literature [27].

In the case of constant microstructure, the elastic anisotropy ratio remains relatively stable with a slight decreasing trend. This can be attributed to the decrease in anisotropy at the nanoscale as the interlayer water stiffness increases. On the contrary, the sample with evolving microstructure shows an increase in the elastic anisotropy ratio upon desaturation. The effect of evolving pore aspect ratio dominates the effect of stiffening interlayer water and results in an increase in elastic anisotropy ratio. We highlight that interactions between micromechanisms at the nano- and micro-scale can give rise to evolving anisotropy with the degree of saturation.

3.2 Influence of MPD

In this section, we present a case of rotation of the orientation of anisotropy with the degree of saturation. Illankoon & Okada [43] and Togashi et al. [95] performed ultrasonic velocity tests and uniaxial compression tests, respectively, on samples of Tage tuff. Both studies found that the direction of maximum Young's moduli changes from the bedding normal direction at high saturations to the bedding parallel direction at low saturations. The rotation occurs at around 70% saturation. Togashi et al. suggested that this behavior is caused by the evolution of the micropore microstructure [95]. One possible explanation for the change in anisotropy orientation could be an evolution of the preferred orientation of clay particles in the rock sample during dehydration [107]. We performed numerical simulations of drying of Tage tuff incorporating an evolving MPD.

Tage tuff is a soft sedimentary rock consisting of compacted and welded volcanic ash and dust [4]. Its composition includes clinoptilolite (zeolite), quartz, anorthite (feldspar) and smectite [33]. The constitutive parameters for Tage tuff are presented in Table 1 [91, 96]. We assumed that the sample has no microcracks. Since there is no data of how the preferred orientation of clay particles in Tage tuff evolves with saturation, we assume a simple linear relationship between MPD and saturation:

$$MPD(\psi^w) = 1.4 - 0.8\psi^w. (30)$$

The predicted Young's moduli in the bedding normal and bedding parallel directions are presented in Figure 7. The proposed model can approximately capture the evolution of Young's moduli for Tage tuff. We note that an evolving MPD with saturation can simulate the rotation of the principal orientation of anisotropy, where the direction of large Young's modulus changes from the bedding normal to the bedding parallel direction upon drying. The two Young's moduli are approximately equal at around 70% saturation. Furthermore, the evolution of Young's moduli are not monotonic with drying, In the bedding normal direction, the Young's modulus first decrease when the

Parameter | Value Nanoscale $\overline{\text{SSA (m}^2/\text{g})}|20$ $n \pmod{\mathrm{m}}$ |50| ϕ^n |0.10| μ (GPa) 4 Microscale ϕ^{μ} |0.66|Macroscale $\overline{\phi^M}$ ϕ^{inc} 0.42 K^{inc} (GPa) 38 u^{inc} (GPa) 44 Water retention curve θ_{sat} 0.4 θ_a^{max} |0.02| α (MPa) 0.331.8 |0.02| $m_{\rm ads}$

Table 1. Constitutive parameters for Tage tuff used in shrinkage tests [33, 91, 96]

sample is initially dried, before increasing significantly below a saturation of around 30%. The initial decrease in Young's modulus can be attributed to the rotation of clay particles in the clay matrix, while the increase in Young's modulus at lower saturations can be caused by hardening of the clay particles as the interlayer distance decreases and interlayer forces dominate the macroscopic behavior.

On the other hand, the proposed model does not capture the slight decrease the bedding parallel Young's modulus between saturations of 60 - 100%. It is possible that there are other micro-mechanisms that our model neglects that results in a decrease in both bedding parallel and bedding normal Young's moduli. For example, the formation of dessication cracks could reduce the elastic moduli [91, 110].

3.3 Constant anisotropy

Several authors have reported constant strain anisotropy during drying tests of shales such as Opalinus clay [66] and Callovo-Oxfordian shale [79]. Previously, this has been attributed to a random distribution of the clay particles, resulting in isotropic elastic properties [10, 28]. However, examination of the microstructure of these shales show a strong alignment of the clay particles [109], which suggests that constant anisotropy at the macroscale is a consequence of micromechanisms at multiple scales negating each other. We present a drying test of Callovo-Oxfordian shale to highlight the interactions between

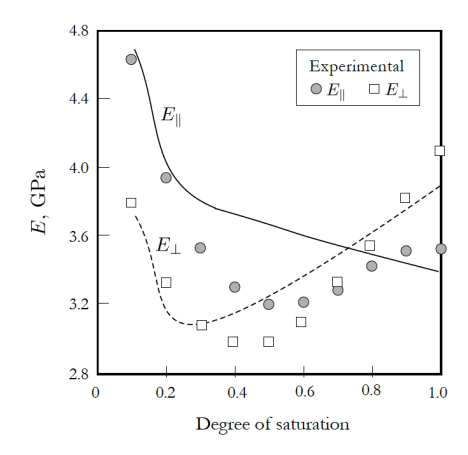


Fig. 7. Variation of Young's moduli with degree of saturation for Tage tuff taken from Illankoon & Osada [43] where a rotation of the direction of maximum Young's moduli occurs. Ticks are data points calculated from ultrasonic velocity measurements; solid and dashed curves are model predictions.

evolving shale microstructure at different scales that give rise to constant strain anisotropy. Numerical simulations of a drying test were performed between the range of saturation from 98% down to 32% saturation. Table 2 presents the constitutive parameters for Callovo-Oxfordian shale used in the drying test [79, 101, 109].

Figure 8 presents the Young's moduli in the bedding normal and bedding parallel directions predicted by the proposed model. Pham et al. [79] measured the bedding normal Young's modulus of their samples at different saturation levels through uniaxial compression tests, which we have also included for comparison. We observe a close match between the bedding normal Young's moduli from experimental data and our model at low saturation levels. Near full saturation, the experimental Young's modulus is lower than that predicted by the model.

The anisotropic strains and strain anisotropy ratio are also presented in Figure 9. Pham et al. measured the strains in the bedding normal and bedding parallel directions [79]. We have presented the measured strains and the calculated strain anisotropy ratio in Figure 9. Our model underestimates the strain in both the bedding normal and bedding parallel directions at high saturation levels. On the other hand, it overestimates the strain in both directions at low saturation levels (around < 50%). Still, the trend in the predicted strain anisotropy ratio follows that of the experimental data. There is little variation in the strain anisotropy ratio with the degree of saturation, as observed in drying tests [79]. We highlight that the material properties used are still strongly anisotropic. The micromechanisms and evolving microstructures

Table 2. Constitutive parameters for Callovo-Oxfordian shale used in shrinkage tests [79, 109]

Parameter	Value
Nanoscale	
SSA (m ² /g)	20
n (mol/m)	50
ϕ^n	0.10
μ (GPa)	13
Microscale	
MPD	3.2
ξ	0.2
ϕ^{μ}	0.19
Macroscale	
ϕ^M	0.015
$\phi^{inc} = \phi^{\text{quartz}} + \phi^{\text{calcite}}$	0.51
$\phi^{ m quartz}$	0.26
$\phi^{ m calcite}$	0.25
K^{quartz} (GPa)	38
μ^{quartz} (GPa)	44
K^{calcite} (GPa)	70
μ^{calcite} (GPa)	32
Water retention curve	
$\overline{ heta_{sat}}$	0.13
$ heta_a^{ ext{max}}$	0.04
α (MPa)	32.7
n	1.98
$m_{ m ads}$	2

at different scales are interacting with one another and negate one another's effects at the macroscale. This gives rise to constant anisotropy.

3.4 Evolving anisotropy

In this section, we investigate the applicability of the proposed homogenization model by comparing against experimental data of evolving anisotropy in Opalinus clay [118]. Yurikov et al. [118] reported the variation of Opalinus clay elastic properties with hydration. Numerical simulations of a shrinkage test were performed between the range of saturation from 100% down to 20% saturation. The constitutive parameters for Opalinus clay at full saturation were estimated from experimental data in the literature and are summarised in Table 3 [30, 48, 101, 109]. We also assume an evolving microstructure of the clay matrix, where the aspect ratio of a pore decreases by 10% upon its drainage.

The model-predicted elastic properites of Opalinus clay is presented and compared to the experimental data from ultrasonic velocities in Figure 10.

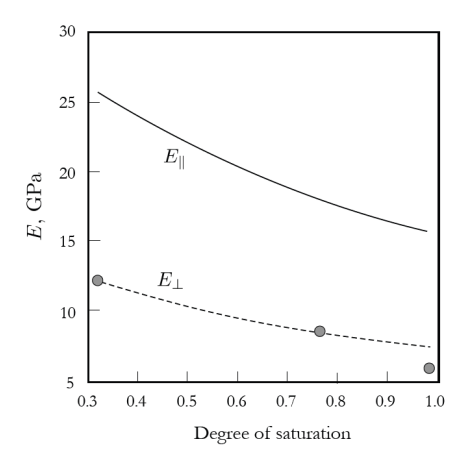


Fig. 8. Variation of anisotropic Young's moduli with degree of saturation for Callovo-Oxfordian shale. Ticks are data points for E_{\perp} from Pham et al. [79]; solid and dashed curves are model predictions.

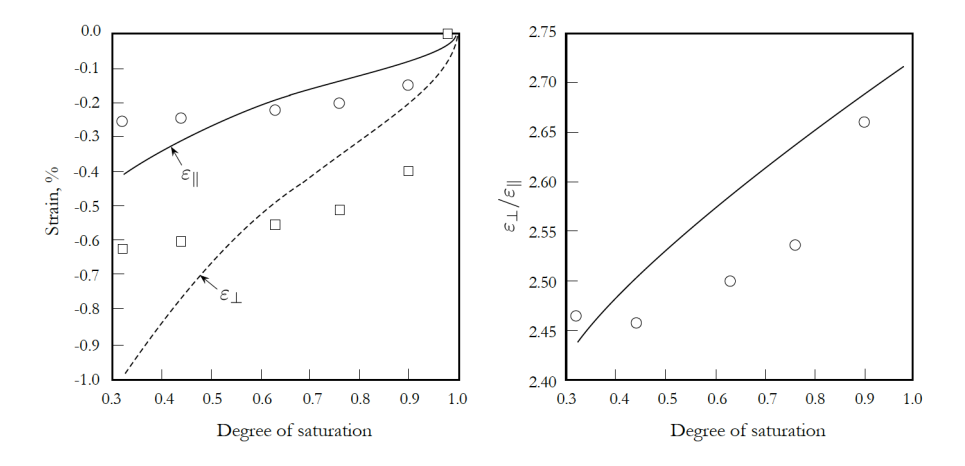


Fig. 9. Predicted anisotropic strains (left) and strain anisotropy ratio (right) induced by desaturation in Callovo-Oxfordian shale. Ticks are data points from Pham et al. [79]; solid and dashed curves are model predictions.

The Young's moduli and shear moduli predicted with the proposed model match well with the experimental data. However, the predicted Poisson's moduli differ significantly from the ultrasonic velocity data. The model predicts generally increasing Poisson's ratios in both the bedding normal and bedding parallel directions during drying. However, the experimental data Poisson's ratio is decreasing in the bedding parallel direction. Furthermore, the bedding normal Poisson's ratio is negative at high saturation ($\psi^w = 0.95$), while our model does not capture this behavior. This may suggest that there are

Table 3. Constitutive parameters for Opalinus clay used in shrinkage tests [30, 48, 101, 109]

_	l	
Parameter	Value	
Nanoscale		
$SSA (m^2/g)$	20	
n (mol/m)	20	
ϕ^n	0.077	
μ (GPa)	20	
Microscale		
MPD	2	
ξ	0.05	
ϕ^{μ}	0.13	
Macroscale		
$\overline{\phi^M}$	0.015	
$\phi^{inc} = \phi^{\text{quartz}} + \phi^{\text{calcite}}$	0.25	
$\phi^{ m quartz}$	0.15	
ϕ^{calcite}	0.10	
K^{quartz} (GPa)	38	
$\mu^{\text{quartz}} (\text{GPa})$	44	
K^{calcite} (GPa)	70	
μ^{calcite} (GPa)	32	
Water retention curve		
$\overline{ heta_{sat}}$	0.15	
$ heta_a^{ ext{max}}$	0.05	
α (MPa)	38.6	
n	1.88	
$m_{ m ads}$	2	

microstructural features that significantly influence the elastic behavior of Opalinus clay that our model does not yet consider.

Notably, there is significant water-weakening of the Opalinus clay sample as bedding parallel Young's moduli doubles between the most saturated state and the driest state. In the proposed model, this is attributed to the closing of microcracks at the macroscale as moisture leaves the sample.

Figure 11 presents the evolution of in-plane and out-of-plane strains during shrinkage. The model predicts anisotropic strains in the sample, with an anisotropy ratio ranging from around 5 at high saturations to around 3.5 at low saturations. This indicates that the proposed homogenization model can capture the evolution in strain anisotropy observed in the literature [67, 80]. We also highlight that the total in-plane strain after desaturation is close to the measured strain of 1.8% [118].

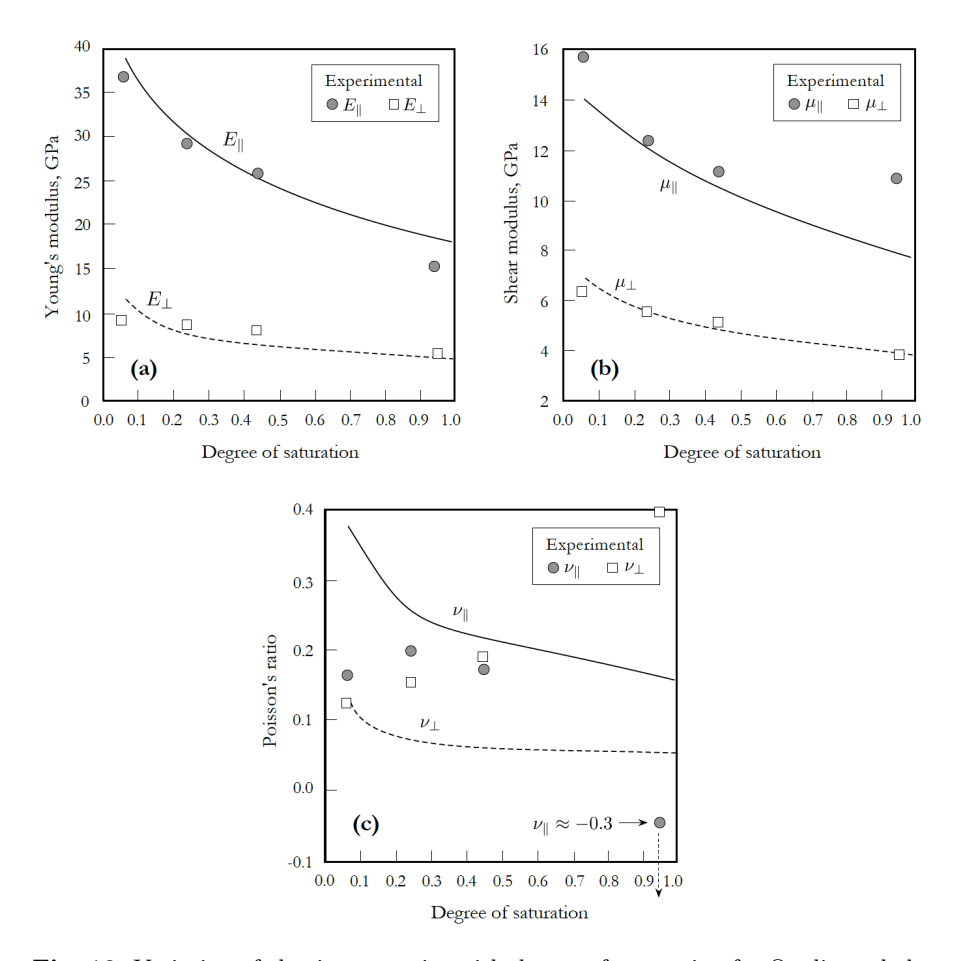


Fig. 10. Variation of elastic properties with degree of saturation for Opalinus shale taken from Yurikov et al. [118]: (a) Young's moduli; (b) shear moduli; (c) Poisson's ratios. Ticks are data points, solid and dashed curves are model predictions.

4 Conclusion

In this study, we have developed a constitutive model for unsaturated clay rocks using a three-level homogenization procedure to account for the micromechanisms occurring at the nano-, micro- and macro-scales. The clay rocks are assumed to consist of clay platelets and interlayer water at the nanoscale, preferentially distributed clay particles and micropores at the microscale, and quartz/calcite inclusions and microcracks at the macroscale. Drying tests of Callovo-Oxfordian shale, Opalinus clay and Tuff tage were simulated using the proposed model to demonstrate its ability to capture the varied drying responses of clay rocks observed in the literature. The results

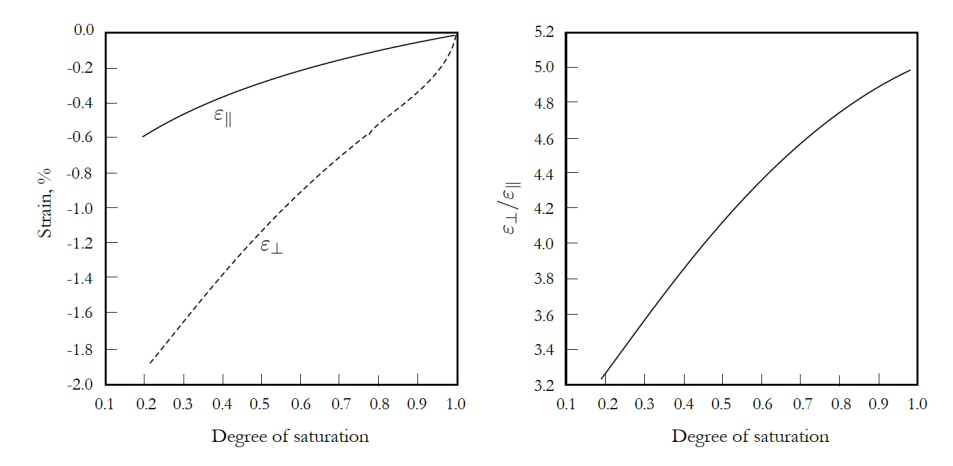


Fig. 11. Predicted anisotropic strains (left) and strain anisotropy ratio (right) induced by desaturation in Opalinus clay.

highlight that the proposed model can capture constant anisotropy, evolving anisotropy and water-weakening of clay rocks.

The proposed homogenization model provides a quantitative link between the evolving microstructure of clay rocks at multiple scales and its macroscopic elastic parameters. With the model, we can begin to quantitatively understand the origin of evolving anisotropy with saturation in clay rocks. Our results highlight that observations in the literature of constant and evolving elastic anisotropy can be attributed to the same interactions between the evolving microstructures of the clay particle and clay matrix. The effects of these micromechanisms on anisotropy at the macroscale can either neutralize each other to give constant anisotropy, or enhance each other to give evolving anisotropy depending on the properties of individual clay rocks. On the other hand, the water-weakening behavior of clay rocks can be attributed to the opening or closing of microcracks at the macroscale upon changes in the degree of saturation. Integrating the proposed model into numerical simulations of applications of clayey rocks, such as tunnel construction [65], underground storage of nuclear waste [31] and anthropogenic CO2 sequestration [105], may provide a deeper and more realistic understanding of the macroscopic mechanical behavior of clavev rocks.

We note that the proposed constitutive model does not consider fluid migration between the pores at different scales. During drying or wetting of the material, the pore fluid is assumed to instantly flow from nanopores out of the rock (drying) or from outside the rock into nanopores (wetting). Further work is underway to incorporate fluid flow between the pore spaces in clay rocks during hydration/dehydration at multiple scales [6, 7, 17, 120] and implement the proposed constitutive model into a numerical simulation code for anisotropic porous media to analyze drying and wetting tests [42, 44].

Appendix A. Hill's tensor

The expression of the Hill's tensor \mathbb{P} for aligned oblate spheroid inclusions and randomly distributed oblate spheroid inclusions used in the proposed homogenization model are presented below. The Hill's tensor characterizes the interaction between the inclusions and the host matrix. It is dependent on the stiffness of the host matrix, the shape of the inclusions and in a transversely isotropic matrix, the orientation of the inclusions in the host matrix.

A1. Aligned oblate spheroidal inclusions

The Eshelby tensor S for an oblate spheroid aligned along the bedding plane in a transversely isotropic host medium was derived by Withers [111].

$$S_{11} = \sum_{i=1}^{2} (2\mathbb{C}_{44}(1+k_{i})\nu_{i}^{2} - \mathbb{C}_{66})A_{i}\nu_{i}I_{1}(\nu_{i})$$

$$+ \frac{D\mathbb{C}_{66}I_{1}(\nu_{3})}{2}$$

$$S_{12} = \sum_{i=1}^{2} (2\mathbb{C}_{44}(1+k_{i})\nu_{i}^{2} - 3\mathbb{C}_{66})A_{i}\nu_{i}I_{1}(\nu_{i})$$

$$- \frac{D\mathbb{C}_{66}I_{1}(\nu_{3})}{2}$$

$$S_{33} = 2\sum_{i=1}^{2} (\mathbb{C}_{13} - \mathbb{C}_{33}k_{i}\nu_{i}^{2})\nu_{i}^{3}k_{i}A_{i}I_{2}(\nu_{i})$$

$$S_{13} = 2\sum_{i=1}^{2} (\mathbb{C}_{13} - \mathbb{C}_{33}k_{i}\nu_{i}^{2})\nu_{i}A_{i}I_{1}(\nu_{i})$$

$$S_{31} = 2\sum_{i=1}^{2} \mathbb{C}_{44}\nu_{i}^{5}k_{i}A_{i}(1+k_{i})I_{2}(\nu_{i})$$

$$- \mathbb{C}_{66}k_{i}\nu_{i}^{3}A_{i}I_{2}(\nu_{i})$$

$$S_{44} = \frac{\mathbb{C}_{44}}{2}\sum_{i=1}^{2} \nu_{i}^{3}A_{i}(1+k_{i})(I_{2}(\nu_{i}) - 2k_{i}I_{1}(\nu_{i}))$$

$$+ \frac{\mathbb{C}_{44}}{4}DI_{2}(\nu_{3})\nu_{3}^{2}$$

where

$$C_{13}^* = \sqrt{C_{11}C_{13}}
\nu_1 = \sqrt{\frac{(C_{13}^* - C_{13})(C_{13}^* + C_{13} + C_{44})}{4C_{33}C_{44}}}
+ \sqrt{\frac{(C_{13}^* + C_{13})(C_{13}^* - C_{13} - C_{44})}{4C_{33}C_{44}}}
\nu_2 = \sqrt{\frac{(C_{13}^* - C_{13})(C_{13}^* + C_{13} + C_{44})}{4C_{33}C_{44}}}
- \sqrt{\frac{(C_{13}^* + C_{13})(C_{13}^* - C_{13} - C_{44})}{4C_{33}C_{44}}}
\nu_3 = \sqrt{\frac{C_{66}}{C_{44}}}
D = \frac{1}{4\pi g_0 \nu_3}
A_1 = -\frac{C_{44} - C_{33}\nu_1^2}{8\pi C_{33}C_{44}(\nu_1^2 - \nu_2^2)\nu_1^2}
A_2 = \frac{C_{44} - C_{33}\nu_2^2}{8\pi C_{33}C_{44}(\nu_1^2 - \nu_2^2)\nu_2^2}
k_i = \frac{C_{11}/\nu_i^2 - C_{44}}{C_{13} + C_{44}}
I_1(\nu_i) = \frac{2\pi \xi}{(\chi_i)^{3/2}} \left(\tan^{-1} \frac{\sqrt{\chi_i}}{\nu_i \xi} - \nu_i \xi \sqrt{\chi_i} \right)
\chi_i = 1 - \nu_i^2 \xi^2$$
(32)

The Hill's tensor can then be expressed as [77]

$$\mathbb{P}_{11} = \frac{\mathbb{S}_{11} - \mathbb{S}_{12}}{2\mathbb{C}_{66}} + \mathbb{P}_{12} \\
\mathbb{P}_{12} = \left(\frac{\mathbb{C}_{33}(\mathbb{S}_{11} + \mathbb{S}_{12}) - 2\mathbb{C}_{13}\mathbb{S}_{33}}{4((\mathbb{C}_{11} - \mathbb{C}_{66})\mathbb{C}_{33} - \mathbb{C}_{13}^2)} - \frac{\mathbb{S}_{11} - \mathbb{S}_{12}}{4\mathbb{C}_{66}}\right) \\
\mathbb{P}_{33} = \frac{(\mathbb{C}_{11} - \mathbb{C}_{66})\mathbb{S}_{33} - \mathbb{C}_{13}\mathbb{S}_{31}}{((\mathbb{C}_{11} - \mathbb{C}_{66})\mathbb{C}_{33} - \mathbb{C}_{13}^2)} \\
\mathbb{P}_{13} = \frac{\mathbb{C}_{33}\mathbb{S}_{31} - \mathbb{C}_{13}\mathbb{S}_{33}}{2((\mathbb{C}_{11} - \mathbb{C}_{66})\mathbb{C}_{33} - \mathbb{C}_{13}^2)} \\
\mathbb{P}_{44} = \frac{\mathbb{S}_{44}}{2\mathbb{C}_{44}} \\
\mathbb{P}_{66} = \frac{\mathbb{S}_{66}}{2\mathbb{C}_{66}} \\$$
(33)

A2. Aligned oblate spheroidal inclusions

The Hill tensor for randomly oriented oblate spheroids in a transversely isotropic host medium is more complex and requires the use of numerical integration to compute [35]. The dilute concentration tensor \mathbb{A}_d can be obtained from the following integration on a unit sphere

$$\overline{\mathbb{A}}_d = \frac{1}{4\pi} \int_{\psi=0}^{2\pi} \int_{\theta=0}^{2\pi} \mathbb{A}_d(\theta, \psi) d\theta d\psi$$
 (34)

where ψ and θ are spherical coordinates and

$$\mathbb{A}_d = (\mathbb{I} + \mathbb{P}(\theta, \psi) : (\mathbb{C}^p - \mathbb{C}^s))^{-1}. \tag{35}$$

The Hill tensor can be expressed as an integration over the spherical coordinates φ and ζ

$$\mathbb{P}_{ijkl} = \int_0^{2\pi} \int_0^{2\pi} (p_l g_{kij} + p_l g_{kji} + p_k g_{lij} + p_k g_{lji}) \sin(\varphi) d\zeta d\varphi$$
(36)

with the following components [29, 35, 75, 111]

$$p_{1} = \frac{\xi^{2} l_{1}}{\eta}$$

$$p_{2} = \frac{(1+\xi^{2}) l_{2} + (1-\xi^{2}) (l_{3} \sin(2\theta) - l_{2} \cos(2\theta))}{2\eta}$$

$$p_{3} = \frac{(1+\xi^{2}) l_{3} + (1-\xi^{2}) (l_{3} \cos(2\theta) + l_{2} \sin(2\theta))}{2\eta}$$
(37)

where

$$\eta = \xi^2 l_1^2 + (l_3 \cos(\theta) + l_2 \sin(\theta))^2
+ \xi^2 (l_2 \cos(\theta) + l_3 \sin(\theta))^2$$
(38)

and

$$\begin{split} g_{111} &= -2\sum_{i=1}^{2} \frac{\nu_{i}A_{i}l_{1}(-8\frac{\nu_{123}}{\rho^{2}} + \frac{\nu_{113}}{R_{i}^{2}} - 3l_{2}^{2} + 2\nu_{i}^{2}l_{3}^{2})}{\rho^{4}R_{i}} \\ &- \frac{Dl_{1}(8\frac{\nu_{233}}{\rho^{2}} + \frac{\nu_{232}}{R_{3}^{2}} - l_{1}^{2} + 2l_{2}^{2} - 2\nu_{3}^{2}l_{3}^{2})}{\rho^{4}R_{3}} \\ g_{112} &= -2\sum_{i=1}^{2} \frac{\nu_{i}A_{i}l_{2}(8\frac{\nu_{i13}}{\rho^{2}} + \frac{\nu_{i13}}{R_{i}^{2}} + 2l_{1}^{2} - l_{2}^{2} - 2\nu_{i}^{2}l_{3}^{2})}{\rho^{4}R_{i}} \\ &- \frac{Dl_{2}(-8\frac{\nu_{313}}{\rho^{2}} + \frac{\nu_{323}}{\rho^{3}} - 3l_{1}^{2} + 2\nu_{3}^{2}l_{3}^{2})}{\rho^{4}R_{3}} \\ g_{113} &= 2\sum_{i=1}^{2} \frac{\nu_{i}^{3}A_{i}l_{3}(2l_{1}^{2} - l_{2}^{2} - \frac{\nu_{i13}}{R_{i}^{2}})}{\rho^{4}R_{3}} \\ &- \frac{D\nu_{3}^{2}l_{3}(l_{1}^{2} - 2l_{2}^{2} + \frac{\nu_{323}}{R_{3}^{2}})}{\rho^{4}R_{3}} \\ g_{121} &= -2\sum_{i=1}^{2} \frac{\nu_{i}A_{i}l_{2}(8\frac{\nu_{i13}}{\rho^{2}} + \frac{\nu_{i13}}{R_{i}^{2}} + 2l_{1}^{2} - l_{2}^{2} - 2\nu_{i}^{2}l_{3}^{2})}{\rho^{4}R_{i}} \\ &+ \frac{Dl_{2}(8\frac{\nu_{313}}{\rho^{2}} + \frac{\nu_{313}}{R_{3}^{2}} + 2l_{1}^{2} - l_{2}^{2} - 2\nu_{3}^{2}l_{3}^{2})}{\rho^{4}R_{i}} \\ g_{123} &= 2\sum_{i=1}^{2} \frac{\nu_{i}^{2}A_{i}l_{1}l_{2}l_{3}(3\rho^{2} + 2\nu_{i}^{2}l_{3}^{2})}{\rho^{4}R_{i}^{3}} \\ g_{131} &= \sum_{i=1}^{2} \frac{\nu_{i}^{2}A_{i}l_{3}(1 - 2\frac{l_{i}^{2}}{\rho^{2}} + \frac{l_{i}^{2}}{R_{i}^{2}})}{\rho^{2}R_{i}} \\ g_{312} &= 2\sum_{i=1}^{2} \frac{k_{i}\nu_{i}^{3}A_{i}l_{1}l_{2}l_{3}(\frac{2}{\rho^{2}} + \frac{l_{i}^{2}}{R_{i}^{2}})}{\rho^{2}R_{i}} \\ g_{313} &= -2\sum_{i=1}^{2} \frac{k_{i}\nu_{i}^{3}A_{i}l_{1}l_{2}l_{3}(\frac{2}{\rho^{2}} + \frac{l_{i}^{2}}{R_{i}^{2}})}{\rho^{2}R_{i}} \\ g_{333} &= \sum_{i=1}^{2} \frac{k_{i}\nu_{i}^{3}A_{i}l_{1}}{R_{i}^{3}} \\ g_{333} &= \sum_{i=1}^{2} \frac{k_{i}\nu_{i}^{3}A_{i}l_{1}}{R_{i}^{3}} \\ \end{cases} R_{i}^{3} \end{aligned}$$

where

$$\rho = \sqrt{l_1^2 + l_2^2}$$

$$R_i^2 = \rho^2 + \nu_i^2 l_3^2$$

$$l_1 = \cos(\zeta) \sin(\varphi)$$

$$l_2 = \sin(\zeta) \sin(\varphi)$$

$$l_3 = \cos(\varphi)$$

$$\bar{\nu}_{imn} = \nu_i^2 l_m^2 l_n^2$$

$$(40)$$

and the remaining variables are the same as in Appendix A1.

Acknowledgements

This work is supported by the U.S. National Science Foundation under Award Number CMMI-1914780.

Data availability statement

The datasets generated during the course of this study are available from the corresponding author upon reasonable request.

References

- [1] Baker DW, Chawla KS, Krizek RJ (1993). Compaction fabrics of pelites: Experimental consolidation of kaolinite and implications for analysis of strain in slate. Journal of Structural Geology, 15(9-10):1123–1137.
- [2] Bennett KC, Berla LA, Nix WD, Borja RI (2015). Instrumented nanoindentation and 3D mechanistic modeling of a shale at multiple scales. Acta Geotechnica, 10(1):1–14.
- [3] Bian K, Liu J, Zhang W, Zheng X, Ni S, Liu Z (2019). Mechanical behavior and damage constitutive model of rock subjected to water-weakening effect and uniaxial loading. Rock Mechanics and Rock Engineering, 52(1):97–106.
- [4] Blatt H, Tracy RJ, Owens BE (2006). Petrology: Igneous, Sedimentary and Metamorphic, 3rd ed. New York, W.H. Freeman and Company.
- [5] Bobko C, Ulm FJ (2008). The nano-mechanical morphology of shale, Mech. Mater., 40:318–337.
- [6] Borja RI (2013). Plasticity Modeling & Computation, Springer, Berlin Heidelberg.
- [7] Borja RI, Choo J (2016). Cam-Clay plasticity, Part VIII: A constitutive framework for porous materials with evolving internal structure. Computer Methods in Applied Mechanics and Engineering 309:653–679.

- [8] Borja RI, Yin Q, Zhao Y (2020). Cam-Clay plasticity. Part IX: On the anisotropy, heterogeneity, and viscoplasticity of shale. Computer Methods in Applied Mechanics and Engineering 360:112695
- [9] Burton GJ, Pineda JA, Sheng D, Airey D (2015). Microstructural changes of an undisturbed, reconstituted and compacted high plasticity clay subjected to wetting and drying. Engineering Geology, 193:363–373.
- [10] Cariou S, Dormieux L, Skoczylas F (2013). An original constitutive law for Callovo-Oxfordian argillite, a two-scale double-porosity material. Applied Clay Science, 80:18–30.
- [11] Carrier B, Wang L, Vandamme M, Pellenq RJM, Bornert M, Tanguy A, Van Damme H (2013). ESEM study of the humidity-induced swelling of clay film. Langmuir, 29(41):12823–12833.
- [12] Casimir HB, Polder D (1948). The influence of retardation on the London-van der Waals forces. Physical Review, 73(4):360.
- [13] Chapman DL (1913). LI. A contribution to the theory of electrocapillarity. The London, Edinburgh, and Dublin philosophical magazine and journal of science, 25(148):475–481.
- [14] Chateau X, Dormieux L (2002). Micromechanics of saturated and unsaturated porous media. International Journal for Numerical and Analytical Methods in Geomechanics, 26(8):831–844.
- [15] Chateau X, Moucheront P, Pitois O (2002). Micromechanics of unsaturated granular media. Journal of Engineering Mechanics 128(8):856–863.
- [16] Chen Q, Nezhad MM, Fisher Q, Zhu HH (2016). Multi-scale approach for modeling the transversely isotropic elastic properties of shale considering multi-inclusions and interfacial transition zone, Int. J. Rock Mech. Min. Sci., 84, 95–104.
- [17] Choo J, White JA, Borja RI (2016). Hydromechanical modeling of unsaturated flow in double porosity media. International Journal of Geomechanics, 16(6):D4016002.
- [18] Choo J, Semnani SJ, White JA (2021). An anisotropic viscoplasticity model for shale based on layered microstructure homogenization. International Journal for Numerical and Analytical Methods in Geomechancs 45(4):502–520.
- [19] Cosenza P, Fauchille AL, Prêt D, Hedan S, Giraud A (2019). Statistical representative elementary area of shale inferred by micromechanics. International Journal of Engineering Science, 142:53–73.
- [20] Cudny M, Staszewska K (2021). A hyperelastic model for soils with stress-induced and inherent anisotropy. Acta Geotechnica 16:1983–2001.
- [21] Day-Stirrat RJ, Flemings PB, You Y, Aplin AC, van der Pluijm BA (2012). The fabric of consolidation in Gulf of Mexico mudstones. Marine Geology, 295:77–85.
- [22] Della Vecchia G, Dieudonné AC, Jommi C, Charlier R (2015). Accounting for evolving pore size distribution in water retention models for compacted clays. International Journal for Numerical and Analytical Methods in Geomechanics, 39(7):702–723.

- [23] Dormieux L, Lemarchand E, Coussy O (2003). Macroscopic and micromechanical approaches to the modelling of the osmotic swelling in clays. Transport in porous media 50(1):75-91.
- [24] Dormieux L, Kondo D, Ulm FJ (2006). Microporomechanics. John Wiley & Sons.
- [25] Dormieux L, Lemarchand E, Sanahuja J (2006). Comportement macroscopique des matériaux poreux à microstructure en feuillets. Comptes Rendus Mécanique, 334(5):304–310.
- [26] Dormieux L, Sanahuja J, Maghous S (2006). Influence of capillary effects on strength of non-saturated porous media. Comptes Rendus Mécanique. 334(1):19–24.
- [27] Douma LA, Dautriat J, Sarout J, Dewhurst DN, Barnhoorn A (2020). Impact of water saturation on the elastic anisotropy of the Whitby Mudstone, United Kingdom. Geophysics, 85(1):MR57–MR72.
- [28] Eghbalian M, Pouragha M, Wan R (2019). Micromechanical approach to swelling behavior of capillary-porous media with coupled physics. International Journal for Numerical and Analytical Methods in Geomechanics, 43(1):353–380.
- [29] Eshelby JD (1961). Elastic inclusion and inhomogeneities. Prog Solid Mech. 2:89–140.
- [30] Ferrari A, Favero V, Marschall P, Laloui L (2014). Experimental analysis of the water retention behaviour of shales. International Journal of Rock Mechanics and Mining Sciences, 72:61–70.
- [31] François B, Laloui L, Laurent C (2009). Thermo-hydro-mechanical simulation of ATLAS in situ large scale test in Boom Clay. Computers and Geotechnics 36(4):626-40.
- [32] Freundlich H (1909), Kapillarchemie; eine Darstellung der Chemie dr Kolloide und verwandter Gebiete, Akademische Verlagsgellschft, Leipzig, Germany.
- [33] Funatsu T, Seto M, Shimada H, Matsui K, Kuruppu M (2004). Combined effects of increasing temperature and confining pressure on the fracture toughness of clay bearing rocks. International Journal of Rock Mechanics and Mining Sciences, 41(6):927–938.
- [34] Ghanbari E, Dehghanpour H (2015). Impact of rock fabric on water imbibition and salt diffusion in gas shales. Int. J. Coal Geol. 138:55–67.
- [35] Giraud A, Huynh QV, Hoxha D, Kondo D (2007). Effective poroelastic properties of transversely isotropic rock-like composites with arbitrarily oriented ellipsoidal inclusions. Mechanics of Materials, 39(11):1006– 1024.
- [36] Griffith CA, Dzombak DA, Lowry GV (2011). Physical and chemical characteristics of potential seal strata in regions considered for demonstrating geological saline CO2 sequestration. Environmental Earth Sciences, 64(4):925–948.

- [37] Gu X, Li Y, Hu J, Shi Z, Liang F, Huang M (2022). Elastic shear stiffness anisotropy and fabric anisotropy of natural clays. Acta Geotechnica 17:3229–3243.
- [38] Guéry AAC, Cormery F, Shao JF, Kondo D (2010). A comparative micromechanical analysis of the effective properties of a geomaterial: effect of mineralogical compositions. Computers and Geotechnics, 37(5):585–593.
- [39] Guo B, Ma L, Tchelepi HA (2018). Image-based micro-continuum model for gas flow in organic-rich shale rock. Advances in Water Resources, 122:70–84.
- [40] Harris NB, Miskimins JL, Mnich CA (2011) Mechanical anisotropy in the Woodford Shale, Permian Basin: Origin, magnitude, and scale. The Leading Edge 30(3):284–291
- [41] Hornby BE, Schwartz LM, Hudson JA (1994). Anisotropic effective-medium modeling of the elastic properties of shales. Geophysics, 59(10):1570–1583.
- [42] Hu D, Zhou H, Zhang F, Shao J, Zhang J (2013). Modeling of inherent anisotropic behavior of partially saturated clayey rocks. Computers and Geotechnics 48:29–40.
- [43] Illankoon TN, Osada M (2016). Effect of saturation level on deformation and wave velocity of a transversely isotropic sedimentary rock. International Journal of the JSRM, 12(1):1–9.
- [44] Ip SCY, Choo J, Borja RI (2021). Impacts of saturation-dependent anisotropy on the shrinkage behavior of clay rocks. Acta Geotechnica, 16(11):3381–3400.
- [45] Ip SCY, Borja RI (2022). Evolution of anisotropy with saturation and its implications for the elastoplastic responses of clay rocks. International Journal for Numerical and Analytical Methods in Geomechanics 46(1):23–46.
- [46] Iwata S, Tabuchi T, Warkentin BP (2020). Soil-water interactions: Mechanisms and applications. CRC Press.
- [47] Johansen TA. Ruud BO, Jakobsen M (2004). Effect of grain scale alignment on seismic anisotropy and reflectivity of shales. Geophysical Prospecting, 52(2):133-149.
- [48] Keller LM, Holzer L, Wepf R, Gasser P (2011). 3D geometry and topology of pore pathways in Opalinus clay: Implications for mass transport. Applied clay science, 52(1-2):85–95.
- [49] Komine H, Ogata N (1996). Prediction for swelling characteristics of compacted bentonite. Canadian geotechnical journal, 33(1):11–22.
- [50] Law BE, Curtis JB (2002). Introduction to unconventional petroleum systems. AAPG bulletin, 86(11):1851–1852.
- [51] Levin VM (1967). On the thermal expansion coefficients of heterogeneous materials. Mechanics of Solids 1:88–94.
- [52] Li B, Wong RC (2017). A mechanistic model for anisotropic thermal strain behavior of soft mudrocks. Engineering Geology, 228:146–157.

- [53] Liu X, Zeng W, Liang L, Xiong J (2016). Experimental study on hydration damage mechanism of shale from the Longmaxi Formation in southern Sichuan Basin, China. Petroleum 2(1):54–60.
- [54] London F (1937). The general theory of molecular forces. Transactions of the Faraday Society, 33:8b–26.
- [55] Loucks RG, Reed RM, Ruppel SC, Hammes U (2012). Spectrum of pore types and networks in mudrocks and a descriptive classification for matrix-related mudrock pores. AAPG bulletin, 96(6):1071–1098.
- [56] Louis L, Day-Stirrat R, Hofmann R, Saxena N, Schleicher AM (2018). Computation of effective elastic properties of clay from X-ray texture goniometry data. Geophysics, 83(5):MR245–MR261.
- [57] Ma L, Fauchille AL, Dowey PJ, Pilz FF, Courtois L, Taylor KG, Lee PD (2017). Correlative multi-scale imaging of shales: a review and future perspectives. Geological Society, London, Special Publications, 454(1):175–199.
- [58] Ma L, Slater T, Dowey PJ, Yue S, Rutter EH, Taylor KG, Lee PD (2018). Hierarchical integration of porosity in shales. Scientific reports, 8(1):1–14.
- [59] Ma T, Wei C, Yao C, Yi P (2020). Microstructural evolution of expansive clay during drying-wetting cycle. Acta Geotech 15:2355–2366.
- [60] Macht F, Eusterhues K, Pronk GJ, Totsche KU (2011). Specific surface area of clay minerals: Comparison between atomic force microscopy measurements and bulk-gas (N₂) and -liquid (EGME) adsorption methods. Applied Clay Science 53(1):20–26.
- [61] Mainka J, Murad MA, Moyne C, Lima SA (2013). A modified form of Terzaghi's effective stress principle of unsaturated expansive clays derived from micromechanical analysis. In Poromechanics V: Proceedings of the Fifth Biot Conference on Poromechanics (pp. 1425–1434).
- [62] March A (1932), Mathematical theory on regulation according to the particle shape in affine deformation: Zeitschrift fur Kristallographie, 81:285–297.
- [63] McLamore R, Gray KE (1967) The mechanical behavior of anisotropic sedimentary rocks. Journal of Engineering for Industry 89(1):62–73.
- [64] Mikhaltsevitch V, Lebedev M, Gurevich B (2018, June). The Effect of Water Saturation on the Elastic Properties of the Wellington Shale at Seismic Frequencies. In 80th EAGE Conference and Exhibition 2018 (Vol. 2018, No. 1, pp. 1-5). European Association of Geoscientists & Engineers.
- [65] Millard A, Bond A, Nakama S, Zhang C, Barnichon JD, Garitte B (2013). Accounting for anisotropic effects in the prediction of the hydromechanical response of a ventilated tunnel in an argillaceous rock. Journal of Rock Mechanics and Geotechnical Engineering 5(2):97-109.
- [66] Minardi A, Crisci E, Ferrari A, Laloui L (2016). Anisotropic volumetric behaviour of Opalinus clay shale upon suction variation. Géotechnique Letters, 6(2):144–148.

- [67] Mishra PN, Zhang Y, Bhuyan MH, Scheuermann A (2020). Anisotropy in volume change behaviour of soils during shrinkage. Acta Geotechnica 15:3399–3414.
- [68] Mitchell JK, Soga K (2005). Fundamentals of soil behavior (Vol. 3, p. USA). New York: John Wiley & Sons.
- [69] Neuzil CE (2013). Can shale safely host US nuclear waste?. Eos, Transactions American Geophysical Union, 94(30):261–262.
- [70] Nemat-Nasser S, Hori M (2013). Micromechanics: overall properties of heterogeneous materials. Elsevier.
- [71] Niandou H, Shao JF, Henry JP, Fourmaintraux D (1997). Laboratory investigation of the mechanical behaviour of Tournemire shale. International Journal of Rock Mechanics and Mining Sciences, 34(1):3–16.
- [72] Niemunis A, Staszewska K (2022). Pure cross-anisotropy for geotechnical elastic potentials. Acta Geotechnica 17:1699–1717.
- [73] Novich BE, Ring TA (1984). Colloid stability of clays using photon correlation spectroscopy. Clays and clay minerals, 32(5):400–406.
- [74] Ortega JA, Ulm FJ, Abousleiman Y (2007). The effect of the nanogranular nature of shale on their poroelastic behavior. Acta Geotechnica, 2(3):155–182.
- [75] Ortega JA, Ulm FJ, Abousleiman Y (2010). The effect of particle shape and grain-scale properties of shale: A micromechanics approach. International Journal for Numerical and Analytical Methods in Geomechanics, 34(11):1124–1156.
- [76] Owens WH (1973). Strain modification of angular density distributions: Tectonophysics, 16:249–261.
- [77] Parnell WJ (2016). The Eshelby, Hill, moment and concentration tensors for ellipsoidal inhomogeneities in the Newtonian potential problem and linear elastostatics. Journal of Elasticity, 125(2):231–294.
- [78] Pervukhina M, Gurevich B, Golodoniuc P, Dewhurst DN (2011). Parameterization of elastic stress sensitivity in shales. Geophysics 76:WA147–WA155.
- [79] Pham QT, Vales F, Malinsky L, Minh DN, Gharbi H (2007). Effects of desaturation—resaturation on mudstone. Physics and Chemistry of the Earth, Parts A/B/C, 32(8-14):646–655.
- [80] Prime N, Levasseur S, Miny L, Charlier R, Léonard A, Collin F (2015). Drying-induced shrinkage of Boom clay: an experimental investigation. Canadian Geotechnical Journal 53(3):396–409.
- [81] Revil A, Lu N (2013). Unified water isotherms for clayey porous materials. Water Resources Research, 49(9):5685–5699.
- [82] Sarout J, Esteban L, Delle Piane C, Maney B, Dewhurst DN (2014). Elastic anisotropy of Opalinus Clay under variable saturation and triaxial stress. Geophysical Journal International 198(3):1662–1682.
- [83] Sayers CM (1994). The elastic anisotropy of shales: Journal of Geophysical Research-Solid Earth, 99:767–774.

- [84] Seiphoori A, Ferrari A, Laloui L (2014). Water retention behaviour and microstructural evolution of MX-80 bentonite during wetting and drying cycles. Géotechnique, 64(9):721-734.
- [85] Semnani SJ, White JA, Borja RI (2016). Thermoplasticity and strain localization in transversely isotropic materials based on anisotropic critical state plasticity. International Journal for Numerical and Analytical Methods in Geomechanics 40(18):2423–2449.
- [86] Semnani SJ, Borja RI (2017). Quantifying the heterogeneity of shale through statistical combination of imaging across scales. Acta Geotechnica 12:1193–1205.
- [87] Semnani SJ, White JA (2020). An inelastic homogenization framework for layered materials with planes of weakness. Computer Methods in Applied Mechanics and Engineering, 370:113221.
- [88] Sevostianov I, Vernik L (2021). Micromechanics-based rock-physics model for inorganic shale. Geophysics, 86(2):MR105–MR116.
- [89] Shen WQ, Shao JF (2015). A micromechanical model of inherently anisotropic rocks. Computers and Geotechnics, 65:73–79.
- [90] Simms PH, Yanful EK (2001). Measurement and estimation of pore shrinkage and pore distribution in a clayey till during soil-water characteristic curve tests. Canadian Geotechnical Journal, 38(4):741–754.
- [91] Soe AKK, Osada M, Takahashi M, Sasaki T (2009). Characterization of drying-induced deformation behaviour of Opalinus Clay and tuff in no-stress regime. Environmental geology, 58(6):1215–1225.
- [92] Sone H, Zoback MD (2013). Mechanical properties of shale-gas reservoir rocks—Part 1: Static and dynamic elastic properties and anisotropy. Geophysics, 78(5):D381–D392.
- [93] Stavropoulou E, Andò E, Tengattini A, Briffaut M, Dufour F, Atkins D, Armand G (2019) Liquid water uptake in unconfined Callovo Oxfordian clay-rock studied with neutron and X-ray imaging. Acta Geotech 14:19–33.
- [94] Sun H, Mašín D, Najser J, Neděla V, Navrátilová E (2020). Fractal characteristics of pore structure of compacted bentonite studied by ESEM and MIP methods. Acta Geotechnica, 15(6):1655–1671.
- [95] Togashi Y, Imano T, Osada M, Hosoda K, Ogawa K (2021). Principal strain rotation of anisotropic tuff due to continuous water-content variation. International Journal of Rock Mechanics and Mining Sciences, 138:104646.
- [96] Togashi Y, Mizuo K, Osada M, Yamabe T, Kameya H (2022). Evaluating changes in the degree of saturation in excavation disturbed zones using a stochastic differential equation. Computers and Geotechnics, 143:104598.
- [97] Ulm FJ, Delafargue A, Constantinides G (2005). Experimental microporomechanics. In Applied micromechanics of porous materials (pp. 207–288). Springer, Vienna.

- [98] Valès F, Minh DN, Gharbi H, Rejeb A (2004). Experimental study of the influence of the degree of saturation on physical and mechanical properties in Tournemire shale (France). Applied Clay Science, 26:197–207.
- [99] Van Genuchten MT (1980). A closed-form equation for predicting the hydraulic conductivity of unsaturated soils. Soil Science Society of America Journal 44:892–898.
- [100] Vasarhelyi B, Ledniczky K (1997). Constitutive equations for rocks under three-point bending load. Acta Technica, 108(1997–99):581–598.
- [101] Vasin RN, Wenk HR, Kanitpanyacharoen W, Matthies S, Wirth R (2013). Elastic anisotropy modeling of Kimmeridge shale. Journal of geophysical research: solid earth, 118(8):3931–3956.
- [102] Vernik L, Nur A (1992). Ultrasonic velocity and anisotropy of hydrocarbon source rocks. Geophysics, 57(5):727–735.
- [103] Vernik L, Anantharamu V (2020). Estimating the elastic properties of mica and clay mineralsElastic properties of mica and clay minerals. Geophysics, 85(2):MR83–MR95.
- [104] Wan M, Delage P, Tang AM, Talandier J (2013). Water retention properties of the Callovo-Oxfordian claystone. Int. J. Rock Mech. Min. Sci. 64:96–104.
- [105] Wang JG, Ju Y, Gao F, Peng Y, Gao Y (2015). Effect of CO2 sorptioninduced anisotropic swelling on caprock sealing efficiency. Journal of Cleaner Production 103:685-95.
- [106] Wei X, Duc M, Hattab M, Reuschlé T, Taibi S, Fleureau JM (2017). Effect of decompression and suction on macroscopic and microscopic behavior of a clay rock. Acta Geotechnica, 12(1):47–65.
- [107] Wei X, Hattab M, Fleureau JM, Hu R (2013). Micro-macro-experimental study of two clayey materials on drying paths. Bulletin of Engineering Geology and the Environment, 72(3):495–508.
- [108] Wenk HR, Lonardelli I, Franz H, Nihei K, Nakagawa S (2007). Preferred orientation and elastic anisotropy of illite-rich shale. Geophysics, 72(2):E69–E75.
- [109] Wenk HR, Voltolini M, Mazurek M, Van Loon LR, Vinsot A (2008). Preferred orientations and anisotropy in shales: Callovo-Oxfordian shale (France) and Opalinus Clay (Switzerland). Clays Clay Miner. 56:285–306
- [110] Wild KM, Wymann LP, Zimmer S, Thoeny R, Amann F (2015). Water retention characteristics and state-dependent mechanical and petrophysical properties of a clay shale. Rock Mechanics and Rock Engineering, 48(2):427–439.
- [111] Withers PJ (1989). The determination of the elastic field of an ellipsoidal inclusion in a transversely isotropic medium, and its relevance to composite materials. Philosophical Magazine A, 59(4):759–781.
- [112] Wong LNY, Maruvanchery V, Liu G (2016). Water effects on rock strength and stiffness degradation. Acta Geotechnica, 11(4):713–737.

- [113] Yang DS, Bornert M, Chanchole S, Gharbi H, Valli P, Gatmiri B (2012). Dependence of elastic properties of argillaceous rocks on moisture content investigated with optical full-field strain measurement techniques. International Journal of Rock Mechanics and Mining Sciences, 53:45–55.
- [114] Yanuka M, Dullien FAL, Elrick DE (1986). Percolation processes and porous media: I. Geometrical and topological model of porous media using a three-dimensional joint pore size distribution. Journal of colloid and interface science, 112(1):24–41.
- [115] Yanuka M (1989). Percolation processes and porous media: III. Prediction of the capillary hysteresis loop from geometrical and topological information of pore space. Journal of colloid and interface science, 127(1):48–58.
- [116] Yin Q, Liu Y, Borja RI (2021). Mechanisms of creep in shale from nanoscale to specimen scale. Computers and Geotechnics 136:104138
- [117] Yong RN, Warkentin BP (1975). Soils Properties and Behavior, Elsevier.
- [118] Yurikov A, Lebedev M, Pervukhina M, Gurevich B. (2019). Water retention effects on elastic properties of Opalinus shale. Geophysical Prospecting, 67(4):984–996.
- [119] Zhang F, Xie SY, Hu DW, Shao JF, Gatmiri B (2012). Effect of water content and structural anisotropy on mechanical property of claystone. Applied Clay Science 69:79–86.
- [120] Zhang Q, Choo J, Borja RI (2019). On the preferential flow patterns induced by transverse isotropy and non-Darcy flow in double porosity media. Computer Methods in Applied Mechanics and Engineering 353:570–592.
- [121] Zhang Q, Fan X, Chen P, Ma T, Zeng F (2020). Geomechanical behaviors of shale after water absorption considering the combined effect of anisotropy and hydration. Engineering Geology 269:105547.
- [122] Zhang Y, Xie L, Zhao P, He B (2020). Study of the quantitative effect of the depositional layering tendency of inclusions on the elastic anisotropy of shale based on two-step homogenization. Geophysical Journal International, 220(1):174–189.
- [123] Zhang Q, Borja RI (2021). Poroelastic coefficients for anisotropic single and double porosity media. Acta Geotechnica 16(10):3013–3025.
- [124] Zhao Y, Semnani SJ, Yin Q, Borja RI (2018). On the strength of transversely isotropic rocks. International Journal for Numerical and Analytical Methods in Geomechanics 42(16):1917–1934.
- [125] Zhao Y, Borja RI (2020). A continuum framework for coupled solid deformation—fluid flow through anisotropic elastoplastic porous media. Computer Methods in Applied Mechanics and Engineering 369:113225.
- [126] Zhao Y, Borja RI (2021). Anisotropic elastoplastic response of doubleporosity media. Computer Methods in Applied Mechanics and Engineering 380:113797.

- [127] Zhao Y, Borja RI (2022). A double-yield-surface plasticity theory for transversely isotropic rocks. Acta Geotechnica, https://doi.org/10.1007/s11440-022-01605-6.
- [128] Zhou Z-h, Wang H-n, Jiang M-j (2021). Macro- and micro-mechanical relationship of the anisotropic behaviour of a bonded ellipsoidal particle assembly in the elastic stage. Acta Geotechnica 16:3899–3921.